

Current effects on wind generated waves near an Ocean Eddy Dipole

Nelson Violante-Carvalho^a, Thiago de Paula^{a,b}, Leandro Calado^c, Felipe Marques dos Santos^d, Luiz Mariano Carvalho^e, Andre Luiz Cordeiro dos Santos^f, Wilton Z. Arruda^g, Leandro Farina^h

^a*Ocean Engineering Program, Rio de Janeiro Federal University (COPPE-UFRJ), Brazil,*

^b*Department of Oceanic Engineering Technology, Petrobras Research and Development Center (CENPES), Brazil,*

^c*Admiral Paulo Moreira Marine Studies Institute, Brazilian Navy (IEAPM), Brazil,*

^d*Marine Autonomous and Robotic Systems, National Oceanography Centre Southampton (NOCS), UK,*

^e*Mathematics Institute, Rio de Janeiro State University (UERJ), Brazil,*

^f*Mathematics Institute, Federal Center for Technological Education of Rio de Janeiro (CEFET-RJ), Brazil,*

^g*Mathematics Institute, Rio de Janeiro Federal University (UFRJ), Brazil,*

^h*Institute of Mathematics and Statistics, Federal University of Rio Grande do Sul (UFRGS), Brazil,*

Abstract

Ocean eddy dipoles are among the most common mesoscale features and may be ubiquitous across the global oceans. However, wave-current interactions in their proximity have not been extensively studied. Here we examine the impact of surface currents on the wave field near an ocean eddy dipole. Using the WW3 wave model, we conducted idealized numerical simulations to assess the influence of different configurations on the spatial variability of Significant Wave Height (H_s). Additionally, a two-month hindcast of a strong dipole event in the Southwestern Atlantic Ocean was performed using three distinct surface current products: SSalto/Duacs, HYCOM NCODA and GlobCurrent. Among these, HYCOM, which incorporates ageostrophic effects, provided a more detailed representation of oceanic energy compared to GlobCurrent and SSalto/Duacs, which primarily reflect geostrophic components. The hindcast assessment employed denoised altimeter-derived H_s data, with a spatial resolution of approximately 6 km. The greatest increase in wave energy occurs in the region between the peak values of positive and

negative vorticity, where the opposing surface currents reach their maximum intensity. Therefore, dipoles act as converging lenses for surface waves, channeling their refraction towards the central jet. Despite its poorer spatial and temporal resolutions, SSalto-Duacs surface current data provides more reliable H_s fields, in the study region where geostrophic dynamics are expected to be significant or even dominant. Both Absolute Dynamic Topography derived surface current inputs produce comparable effects on the wave field, with the inclusion of the Ekman component yielding no substantial enhancement. HYCOM captures a broader range of dynamical processes, essential for accurately representing the total energy, though discrepancies with SSalto/-Duacs data may arise from assimilation inaccuracies and model limitations. While gridded altimetry may underestimate total current components during dipole events, it offers precise insights into their positioning and evolution, useful for specific event analysis and near real-time forecasting for marine safety.

Keywords: Effects of currents on waves, Ocean Eddy Dipole, wave spectra, surface current input.

1. Introduction

Wind generated waves are affected by underlying currents and this interaction becomes particularly complex in the vicinity of ocean eddy dipoles. These mesoscale features, characterized by rotating currents with opposing polarities, can significantly influence wave propagation and dynamics, including changes in wave period, direction and energy distribution. Understanding how currents modify waves within eddy dipoles is crucial for ocean engineering, ship routing and hazard assessments. Additionally, studying current effects on waves can provide insights into broader air-sea momentum exchange processes and their role in ocean circulation patterns (Benetazzo et al., 2013; Marechal and Ardhuin, 2021; Altiparmaki et al., 2024).

Wave-current interactions have been investigated in recent studies, including, among others, Ardhuin et al. (2012, 2017); Quilfen et al. (2018a); Romero et al. (2017, 2020); Bôas et al. (2020); Lauton et al. (2023). The change of wave height induced by surface currents depends on their relative velocities — if the group velocity of the waves is much larger than the current speed, the waves will propagate unaffectedly. However, if the surface current speed is a considerable fraction of the group velocity, the waves will

be advected and hence their propagation will be affected by the current. Onorato et al. (2011) demonstrated with numerical simulations, employing a modified nonlinear Schrodinger equation, that the maximum amplitude of monochromatic waves in opposing currents can increase significantly when the ratio between surface current speed and group velocity is in the range 0.1 to 0.4. For relative larger currents, and therefore larger ratios, wave breaking and blocking might occur. Currents can modify the direction of wave propagation at a given location through the combined effects of refraction and wave action advection. The degree of deviation from great circle paths is not directly dependent on the surface current speed but rather on the ratio between the vertical component of vorticity and the group velocity.

The primary dynamic component of surface circulation in the South Brazilian Bight is the Brazil Current (BC), a western boundary current that completes the wind-driven South Atlantic Subtropical Gyre. As it flows south-southwestward along the continental slope, the BC exhibits a pronounced meandering pattern that frequently encloses eddies. These eddies are primarily generated by flow-topography interactions and baroclinic instability (Silveira et al., 2008; Rocha et al., 2014; Silveira et al., 2023). Recurrent eddy-like features have been documented along the entire path of the BC, from its genesis near 15°S to the Brazil–Malvinas Confluence at 39°S (Biló et al., 2014). The most persistent eddies are typically observed off Vitória (20°S), Cabo de São Tome (22°S), and Cabo Frio (23°S) (Calado et al., 2006). In the region where the Cabo Frio Eddy forms (around 23°S), the BC encounters a significant change in coastline orientation, shifting from a southwest to a westward direction over a span of a few tens of kilometers. Due to its inertia, the BC veers away from the shelf break and is displaced to greater depths. This displacement leads to the acquisition of cyclonic relative vorticity as the current conserves its potential vorticity (Campos et al., 2000). The resulting cyclonic circulation at this location occasionally couples with westward-propagating anticyclonic features, resulting in the formation of an eddy dipole structure. This structure is characterized by a strong intensification of surface currents in its central region (de Paula et al., 2021). The dipoles formed in this area commonly propagate south-southwestward, substantially altering local surface circulation patterns.

One of the defining characteristics of ocean eddy dipoles is the formation of a central jet, characterized by its high velocity and narrow width, see a schematic representation over the South Brazilian Bight in Figure 1. When the eddies are in close proximity, their rotational flows converge, creating

a narrow, intense current between them. The central jet typically exhibits higher velocities compared to the surrounding eddy flows — the speed of the jet can reach up to several tens of centimeters per second, depending on the intensity and size of the eddies. Ni et al. (2020) pointed out that dipoles are widespread in the global ocean, with about 30–40% of the mesoscale eddies identified in altimeter data as dipoles — the percentage is even higher in energetic regions such as the Gulf Stream and the Southern Ocean.

Dipoles create complex spatial variations in the surface current field, leading to wave refraction. As waves propagate through the variable flow fields of the cyclonic and anticyclonic eddies, their trajectories bend according to the changes in current velocity and direction. This refraction can lead to wave focusing or defocusing, depending on the relative orientation of the waves and the dipole. The wave focusing effect, particularly along the central jet, can result in increased wave heights and energy concentration.

We examine the response of the spatial variability of the wave field to the surface currents in the vicinity of an eddy dipole employing remote sensing data and numerical models. As a first approach, we analyze an idealized setup employing the numerical wave model WAVEWATCH III (WW3, see WW3DG, 2019) forced by realistic surface currents to discuss how the significant wave height (H_s) field is affected. Additionally, a two-month hindcast of a very intense dipole event is examined, with three distinct surface current fields used as input to the WW3 wave model in the Southwestern Atlantic Ocean, a region known for the recurrent occurrence of dipoles. The Hybrid Coordinate Ocean Model (HYCOM) relies on simulations driven by physical equations, whereas GlobCurrent and SSalt integrates observational data from satellites. The latter two are derived from altimeter data and therefore the surface fields include only the geostrophic component — plus the Ekman component added in the GlobCurrent product. Numerical models, such as HYCOM, are also essential for incorporating ageostrophic effects not present in the altimeter data. Each of the three surface current products differs in terms of methodologies, data sources, (spatial and temporal) resolutions and applications. We discuss the impacts of using these distinct products as input to the hindcasts of the wave field.

2. The Effects of Currents on Waves in the Vicinity of Eddy Dipoles

Peregrine (1976) highlighted the occurrence of frequency Doppler shift when waves propagate over currents, discussing the interplay between the

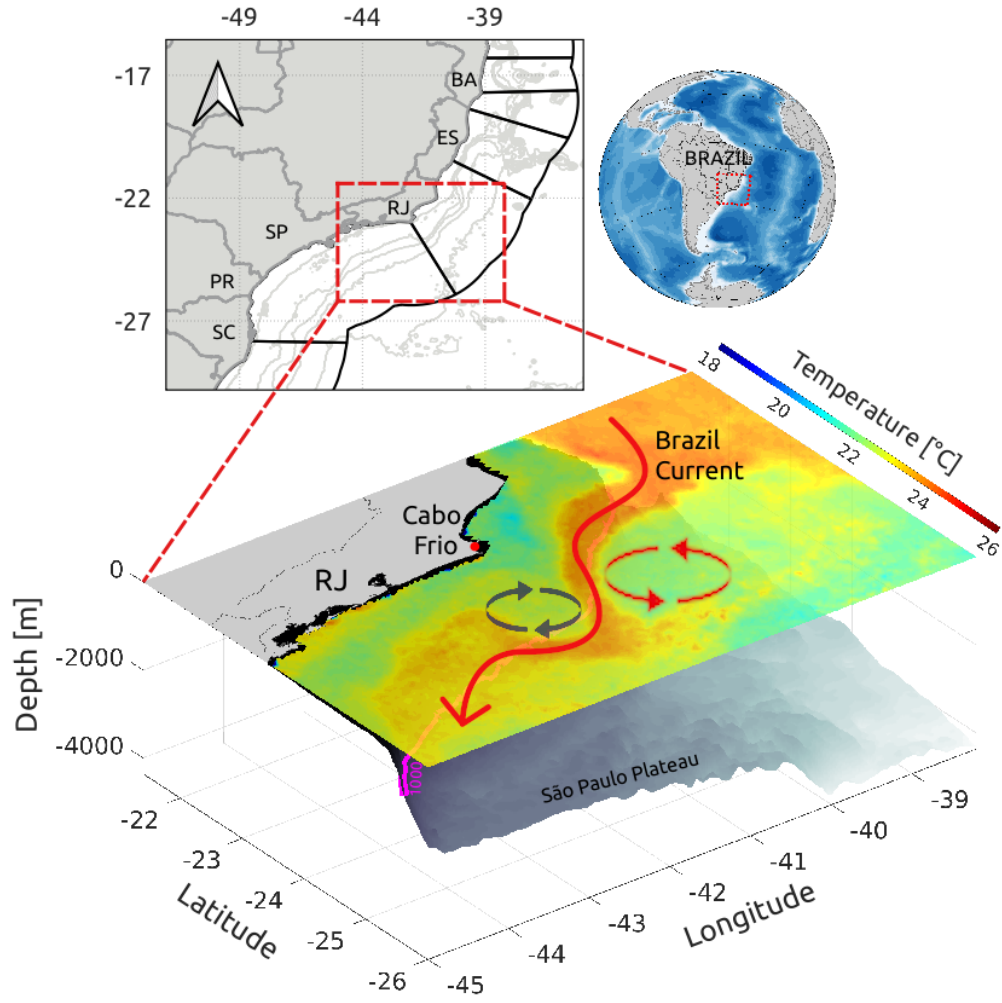


Figure 1: Key topographic features and main surface circulation with an example of a typical dipole composed of a cyclonic eddy (black) and an anticyclonic eddy (red).

intrinsic frequency of the wave and the relative motion induced by the current, in the form

$$\omega = \sigma + \mathbf{k} \cdot \mathbf{U}. \quad (1)$$

The absolute frequency as observed from a fixed reference frame is ω , σ is the intrinsic frequency when observed from a moving reference frame, \mathbf{k} is

the wavenumber vector and $\mathbf{U} = \mathbf{U}(t, \mathbf{x})$ represents the horizontal surface current, with t denoting time and \mathbf{x} representing the position vector.

The temporal changes in the current field occur at a rate much slower than that of propagating waves. Therefore, the temporal scales of the current field are significantly longer than the corresponding wave scales. The assumption extends to the spatial domain, with scales associated with current variations significantly larger than that of the waves, hence

$$k \gg \max \left| \frac{1}{U} \frac{\partial U}{\partial x} \right| \quad \text{and} \quad \omega \gg \max \left| \frac{1}{U} \frac{\partial U}{\partial t} \right|. \quad (2)$$

Equation (1) underscores the dynamic nature of wave propagation over currents. The term $\mathbf{k} \cdot \mathbf{U}$ denotes the influence of the current velocity on the wave frequency and could be perceived as a Doppler shift; when current and wave propagate in the same direction ($\mathbf{k} \cdot \mathbf{U} > 0$), the waves are stretched — conversely, if the current opposes the wave direction, the waves become shorter. When the waves propagate orthogonally to the current, no influence is observed.

The relation between the intrinsic frequency and the wavenumber of a uniform plane wave of infinitesimal amplitude, propagating over still water of uniform depth h relies upon the dispersion relationship

$$\sigma^2 = gk \tanh kh, \quad (3)$$

where g is the gravitational acceleration and $k = \|\mathbf{k}\|_2$. On the surface of a uniform current, the dispersion relation (3), using Equation (1), turns into

$$(\omega - \mathbf{k} \cdot \mathbf{U})^2 = gk \tanh kh. \quad (4)$$

Considering the particular case of waves collinear with currents, the amplitude in the presence of currents (a) and the amplitude without currents (a_0) have the ratio (Phillips, 1977)

$$\frac{a}{a_0} = \frac{c_0}{\sqrt{(2U + c)c}}, \quad (5)$$

where c and c_0 are, respectively, phase speed with or without currents. To illustrate, a 15 s period wave propagating over a 1 ms^{-1} opposing current can result in a 10% amplification in wave height. In the same scenario, this

is enhanced to around 25% for a wave with a shorter 7 s period — naturally, stronger opposing currents result in stronger amplifications. Hence, opposing waves near the dipole central jet are expected to increase in height and steepness (Onorato et al., 2002; Toffoli et al., 2015). The wave amplification increases rapidly to opposing current velocities — the slower the waves and the stronger the currents, the steeper the curve.

Kenyon (1971) discussed the possible causes, later supported by several simulations presented by Gallet and Young (2014), of the discrepancies reported by Munk et al. (1963) in their work about swell propagation over large distances. For instance, islands could block and diffract swell energy away from great circle propagation (Violante-Carvalho et al., 2021) — and ocean currents could potentially be accounted for by causing refraction (Moreira and Peregrine, 2012). Currents can alter the direction of wave propagation at a specific location through both the processes of refraction and advection of wave action, not included in the analysis by Munk et al. (1963).

The amount of bending from great circles is not function of the surface current speed itself, but of the ratio between the vertical component of the vorticity (ζ) and wave group velocity (c_g):

$$\chi = \frac{\zeta}{c_g} + \mathcal{O}(e^2), \quad (6)$$

where χ is the ray curvature, $\zeta = \frac{\partial v}{\partial x} - \frac{\partial u}{\partial y}$, $\mathbf{U} = (u, v)$ the current velocity and $e = \|\mathbf{U}\|_2/c_g$ — see a thorough discussion in Kenyon (1971) and Dysthe (2001) considering predictions from ray theory. Slower, shorter waves are, therefore, more refracted. Moreover, the bending direction follows the signal of the vorticity field — positive vorticity causes waves to bend to the left and negative to the right — and the bending increases with increasing current vertical vorticity. Therefore, an eddy dipole acts like a focal lens by bending waves that oppose the central jet’s current, effectively redirecting them toward the jet. The combined influence of refraction and advection over the central jet leads to a more substantial increase in wave energy compared to the effects of refraction and advection acting independently.

3. Data

3.1. Surface Current Fields

3.1.1. Surface Current Field Employed in the Idealized Simulations

A realistic surface field from a HYCOM snapshot of 08-Sep-2010 07:00:00 was employed, see Figure 2a. The selection is based on the occurrence of an intense dipole in the Sao Paulo Plateau, where ocean currents frequently intensify. Furthermore, this is a particularly interesting selection for idealized simulations because the central jet presents a very well defined and straight North-South orientation. This event is thoroughly discussed in de Paula et al. (2021), with speed comparisons between a regional simulation using ROMS and two global reanalyses — GLORYS and HYCOM — against mooring measurements positioned on the central axis of the dipole. The results demonstrated that HYCOM was capable of reproducing the magnitude of the currents, greater than 1 ms^{-1} . The velocity field was used as a series of static snapshots — without temporal evolution — to drive the wave model with horizontal resolution of $1/12^\circ$ ($\sim 9 \text{ km}$) and temporal resolution of one hour. The steady state conditions eliminate the need to account for transient effects and time-varying behavior, therefore simplifying the analysis.

3.1.2. Surface Current Field Employed in the Two-Month Hindcast

Three distinct surface current fields were employed as input for the wave model hindcasts, comprising the period of August and September 2010. The main differences between SSalto/Duacs, HYCOM NCODA and GlobCurrent lie in the methods and data sources used to derive these fields — and consequently their spatial and temporal resolution, accuracy and typical applications.

The SSalto/Duacs from AVISO (Archiving, Validation and Interpretation of Satellite Oceanographic data — www.aviso.altimetry.fr) gridded product is a dataset with horizontal resolution of $1/4^\circ$ ($\sim 25 \text{ km}$) and temporal frequency of 1 day (Mertz et al., 2023). The dataset results from a Level 4 processing that combines data from multiple satellites — such as TOPEX/Poseidon, Jason-1, Jason-2 and Jason-3 — to produce continuous fields of Absolute Dynamic Topography (ADT). The altimeter exclusively measures surface height and geostrophic currents, thereby omitting subsurface shears and ageostrophic currents. Surface current fields derived from ADT represent

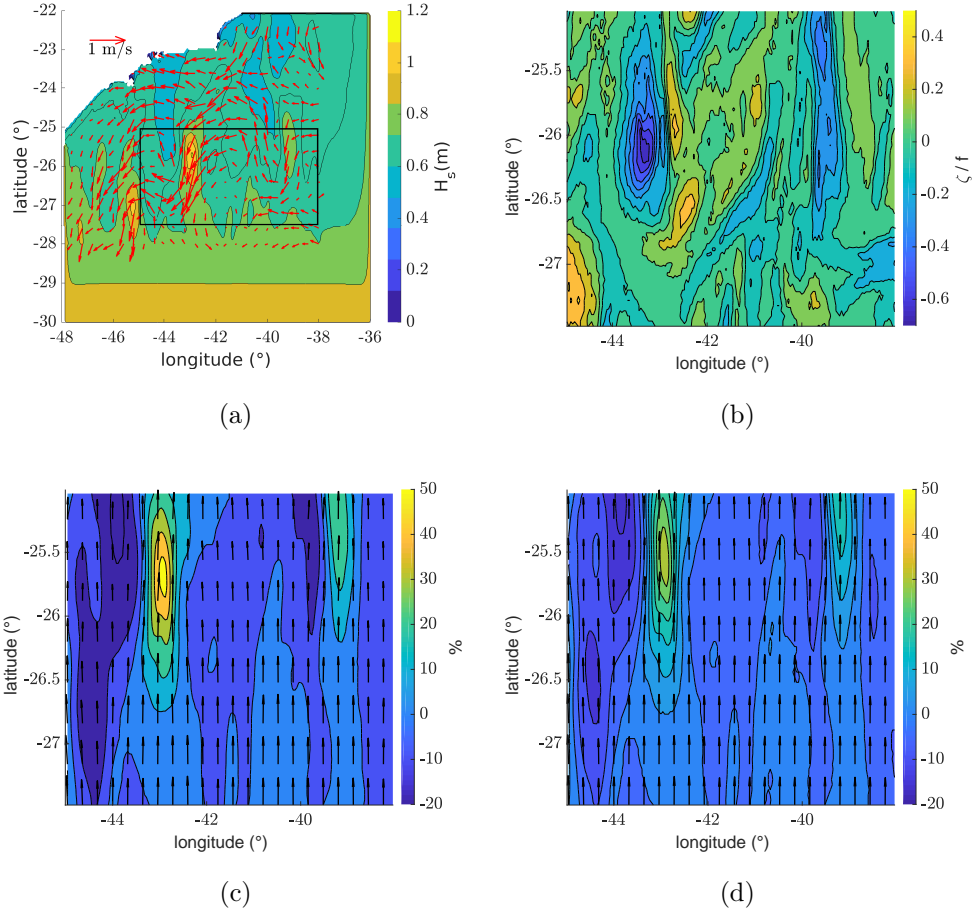


Figure 2: [a] is the map of significant wave height (H_s) for the 7 s waves ($\epsilon = 0.0822$). The arrows indicate the surface current direction and magnitude with its scale displayed at the left top corner. [b] is the Rossby number — the surface relative vorticity ζ normalized by the Coriolis parameter f — in the region shown as a black rectangle in [a]. [c] [d] are the relative difference of H_s , in the black rectangle, between the runs using the current input and the run with no current (respectively for the 7 s and 15 s waves). The arrows indicate wave propagation direction scaled by H_s .

the geostrophic component of ocean currents, represented by (respectively in

the eastward and northward directions)

$$u_g = -\frac{g}{f} \frac{\partial \text{ADT}}{\partial y} \quad (7)$$

and

$$v_g = +\frac{g}{f} \frac{\partial \text{ADT}}{\partial x}, \quad (8)$$

where f is the Coriolis parameter. Therefore, the SSalto/Duacs gridded product is an observational dataset, but it has some uncertainty associated with the gridding process — since along-track data are combined from different time instances to produce a continuous surface current field.

HYCOM (www.HYCOM.org) combines pressure coordinates, isopycnals and sigma coordinates (Fox et al., 2002) which allows for a more accurate representation of ocean dynamics, particularly in areas with significant depth variations. The model has fine spatial and temporal resolution and the ability to simulate complex ocean processes due to its hybrid approach, therefore including meso and submesoscale effects not necessarily captured from altimeter data. However, HYCOM would not have adequate resolution to resolve a considerable portion of the submesoscale with its effects incorporated into the current field through parameterizations (Gula et al., 2022). Here we employed the HYCOM NCODA GOFS 3.1, the most recent reanalysis of global HYCOM with $1/12^\circ$ (~ 9 km) resolution and 41 vertical levels with temporal frequency of 3 hours. The model resolves the primitive equations governing the conservation of momentum, mass and heat, while assimilating observational data on temperature, salinity and surface elevation. HYCOM and most of the global forecasting models assimilate along-track altimetry, hence, part of the data observed in the gridded SSalto/Duacs is being incorporated by HYCOM during assimilation (Chassignet et al., 2006, 2009).

The Ekman component represents the wind-driven part of surface currents, typically in the upper 50-100 meters. Wind stress on the ocean surface creates a drag force that sets the water in motion, which diminishes with depth, following an exponential decay profile. The GlobCurrent product (<http://GlobCurrent.ifremer.fr/>) merges altimetry data with wind fields to generate combined current fields, respectively from SSalto/Duacs maps and the wind stress from ERA Interim (Rio et al., 2014). The surface current fields include both the geostrophic component (\mathbf{u}_g) and the Ekman compo-

ment (\mathbf{u}_{ek}) induced by the local wind shear stress

$$\mathbf{u}_{ek} = \beta(z)\tau e^{i\theta(z)}, \quad (9)$$

where z represents the vertical axis, $\beta(z)$ is vertical diffusivity, τ is the wind stress and $\theta(z)$ is the direction of the Ekman current at different depths. This provides a more comprehensive picture of the surface current field, accounting for both pressure-driven and wind-driven components. With spatial and temporal resolutions of respectively $1/4^\circ$ (~ 25 km) and 3 hours, the accuracy of GlobCurrent is considered high, particularly in regions well covered by satellite data (Cancet et al., 2019). The most significant expected impact of adding the Ekman component is on the magnitude of the surface currents — the wind can enhance or weaken the geostrophic currents. The Ekman component can also influence the direction of surface currents, causing the overall current to veer slightly to the left (in the Southern Hemisphere) compared to the geostrophic current alone. However, the position of mesoscale features (such as the dipole’s central jet) is expected to be generally similar between ADT-derived geostrophic currents and its combination with the Ekman component. Hence, since a significant portion of the current field comes from the geostrophy, it is expected that the GlobCurrent and SSalto/Duacs products will be very similar, with the addition of high frequency variability due to the Ekman component and its 3-hour resolution — in contrast to SSalto’s daily resolution.

Therefore, to summarize. SSalto/Duacs is observational data, HYCOM NCODA is a numerical model of primitive equations (with assimilated altimeter data) and GlobCurrent is a combination of observational data and numerical models. HYCOM is more detailed and suitable for forecasts and dynamic studies, constrained however by the known limitations of any numerical model. On the other hand, SSalto/Duacs and GlobCurrent data are limited to the geostrophic (and combined with Ekman) components of the surface currents for near real time and its historical database spanning over 25 years — they do not have a forecast product as those provided by global and regional numerical models.

3.2. WW3 Wave Model

3.2.1. Idealized Simulations Setup

The idealized simulations were conducted using WW3 version 7.14, with a spectral grid comprising 24 directions ($\Delta\theta = 15^\circ$) and 32 frequencies, expo-

nentially spaced from 0.0373 Hz to 0.7159 Hz with an increment factor of 1.1. The ST4 source term package (Ardhuin et al., 2010) was implemented, configured with $\beta_{max} = 1.55$, as described in WW3DG (2019), which extensively documents the model configuration, governing equations and computed bulk parameters — see also Kaiser et al. (2022) for a discussion about different values of β_{max} in the South Atlantic Ocean. The grid increment was 0.04° (4.4 km) in both Δx and Δy , covering the area from 48°W to 36°W and 30°S to 22°S in the Southwestern Atlantic Ocean — see Figure 2a — employing the ETOPO1 database (Amante and Eakins, 2009).

Waves entered the domain from the southern boundary, about 100 km downwave of the dipole, and propagated northward ($\theta = 180^\circ$). The simulations were conducted over a period of 30 days, allowing sufficient time for the system to reach a steady state within the computational domain. Two initial states of WW3 simulations were considered, with H_s set to 1 m and directional spreading (σ) to 15° . Peak wave periods (T_p) were assigned distinct values of 7 s and 15 s, resulting in corresponding steepness values ($\epsilon = \frac{H_s}{2} k_p$, where k_p is the peak wavenumber) of 0.0822 and 0.0179, respectively.

Therefore, four different runs were analysed — two distinct values of ϵ and the surface current field. Additionally, two control runs without current input were performed for both values of ϵ . Incorporating surface ocean currents into wave simulations reduces wave heights in most regions globally, primarily due to the reduction in relative wind caused by the alignment of winds and currents (Echevarria et al., 2021). Here, to isolate the effects of currents on waves and simplify the analysis, wind input was excluded to eliminate continuous spectral modifications associated with wind forcing. In our simulations, which were characterized by relatively low steepness values, dissipation and nonlinear interactions were considered negligible; however, they were activated in all cases to account for any potential influence on the results.

3.2.2. Hindcast

For the August and September 2010 hindcast, the WW3 version, grid and frequency discretization, configuration and bathymetry employed in the idealized simulations were applied. However, two directional discretizations were employed, the original comprising 24 directions ($\Delta\theta = 15^\circ$) and a higher resolution of 72 directions ($\Delta\theta = 5^\circ$). Eight runs were analyzed, using as input the three surface fields described in Section 3.1.2 and an additional control run with no current, for the two directional discretiza-

tions. The wave model was also driven by hourly wind data from the ERA5 reanalysis dataset, produced by the European Centre for Medium-Range Weather Forecasts (ECMWF), with a spatial resolution of 0.25° (available at <https://cds.climate.copernicus.eu/>). Wave spectra forcing the model at the offshore boundaries were also from ERA5, with 24 directions, 30 frequency bands and a 0.5° grid with hourly temporal resolution.

3.3. Altimeter data from the ESA Sea State Climate Change Initiative

Until recently, the use of altimeter data often required preliminary low-pass filtering, which systematically resulted in the loss of small-scale features (< 100 km) (Marechal and Ardhuin, 2021). In this context, the analysis of H_s spatial variations was limited to wavelengths larger than 100 km, due to the noise associated with the tracking methods used to interpret altimeter waveforms (Sandwell et al., 2014; Ardhuin et al., 2017). To overcome this limitation, the successful application of the Empirical Mode Decomposition (EMD) (Huang et al., 1998) to the denoising of H_s along-track series now makes it possible to investigate much smaller scales, possibly down to 15 km wavelength or less (Quilfen and Chapron, 2019).

In the present work, we use denoised H_s (see details in Huang et al., 1998) from the European Space Agency (ESA) Sea State Climate Change Initiative (SeaState-CCI). In particular, the Level 3 (version 3) data is a global daily merged multi-sensor along-track satellite altimeter H_s at about 6 km spatial resolution from 2002 to 2021 (Piollé et al., 2022). From now on, we will refer to this dataset as CCI-Hs.

The CCI-Hs is based on a complete retracking of multiple satellite altimetry missions: Envisat, CryoSat-2, Jason-1, Jason-2, Jason-3, SARAL and Sentinel-3A. Taking into account that many altimeters are bi-frequency (Ku-C or Ku-S), for consistency reasons, only measurements in Ku band were used (except SARAL, where Ka band was used). The selected tracks employed in the analysis that intersected the eddy dipole region — specifically, those tracks that crossed the dipole’s central jet for the designated date — are listed in Table 1.

Statistical metrics were computed to assess the agreement between altimeter measurements and *in situ* data for each altimeter mission and year (Dodet et al., 2020). The dataset is generated using a high-level denoising method, validation against in-situ measurements and numerical model outputs. In the Sea State CCI version 3, the Jason-2 mission was selected as

Table 1: List of selected tracks that crossed the eddy dipole region. Date is approximately at the center of the track segment.

#	Date	Satellite	Cycle
1	04-Aug-2010 00:47:00	Jason-2	76
2	09-Aug-2010 13:11:00	Jason-2	77
3	04-Sep-2010 12:36:00	Envisat	92
4	08-Sep-2010 07:07:00	Jason-2	80
5	08-Sep-2010 01:01:00	Envisat	92
6	11-Sep-2010 01:07:00	Envisat	92
7	12-Sep-2010 16:41:00	Jason-2	80
8	13-Sep-2010 06:10:00	Jason-1	320
9	14-Sep-2010 01:13:00	Envisat	93
10	18-Sep-2010 05:05:00	Jason-2	81
11	19-Sep-2010 12:39:00	Cryosat-2	2
12	21-Sep-2010 12:37:00	Cryosat-2	2
13	22-Sep-2010 14:40:00	Jason-2	81
14	23-Sep-2010 12:35:00	Cryosat-2	2

reference to inter-calibrate the remaining missions. A first step was to calibrate this reference mission against *in situ* data, considered as the ground truth. In a second step, the remaining missions (namely, Envisat, Jason-1, Saral, CryoSSat-2 and Jason-3) were compared against the calibrated Jason-2 data at crossover locations in order to perform the inter-calibration. The analysis considered only altimeter and *in situ* match-ups occurring more than 200 km from the coast, for the performance of calibrated and denoised altimeter significant wave height data. All missions exhibit a positive bias of less than 10 cm, while the root mean square error remains below 26 cm for all missions, corresponding to a normalized mean value below 11%. Additionally, the scatter index is consistently lower than 9%, while the coefficient of determination exceeds 0.96 for all missions, indicating strong agreement between the datasets. A thorough discussion of the statistical metrics for each mission, including altimeter inter-calibration, long-term trends, cross-consistency analysis, quality assessment and the processing of altimeter data, is presented in Dodet et al. (2020).

4. Results

4.1. Idealized Simulations in the Vicinity of an Eddy Dipole

Figure 2a shows the spatial variability of H_s , considering the 7 s waves. The cyclonic eddy, with negative vorticity and clockwise rotation in the Southern Hemisphere, is more energetic than its anticyclonic pair with positive vorticity. The refraction of the northward waves towards the central jet is hence asymmetric — the amount of bending from great circles is function of the ratio between the vertical component of the vorticity and group velocity (Equation 6). The normalized relative vorticity is displayed in Figure 2b, in the area shown as a black rectangle.

The relative difference in the H_s field between runs with and without current is shown in Figure 2, bottom row. A maximum increase in H_s for the 7 s waves of over 50% is observed in the central jet (Figure 2c, around 43°W and 25.75°S), in the region between the maximum values of positive and negative vorticity, with maximum opposing surface currents of approximately 1 m s^{-1} . Therefore, dipoles function as converging lenses for surface waves, directing their refraction toward the central jet. For comparison, under these conditions, applying the linear theory to a 7 s monochromatic wave in the presence of homogeneous opposing currents predicts an increase of approximately 25% (Equation 5). The combined effects of refraction and advection is responsible for a substantial increase in the wave energy and steepness over the central jet. Similar spatial variability was observed for the 15 s waves (Figure 2d), but with smaller intensification — maximum of 33%. Comparatively, shorter period waves exhibit significant changes in both height and steepness, often resulting in energy dissipation through breaking. Although not discussed in detail here, the directional spreading is also influenced by the dipole, as wave refraction alters their direction and consequently σ . With a narrow wave spectrum, refraction concentrate the wave energy into a tighter area, amplifying its impact. On the other hand, if the wave spectrum is wide, the energy is distributed across a broader area since the various spectral components are more spread out. The narrower the directional spreading, the more marked the alterations, exhibiting substantial broadening along the central jet. Hence, the narrow $\sigma = 15^\circ$ employed in the simulations is expected to cause a pronounced increase in energy.

Recent studies have demonstrated that refraction is the primary factor driving spatial variations of H_s at mesoscale, between 20 and 100 km (Ardhuin et al., 2017; Romero et al., 2017; Quilfen et al., 2018b). More specifically,

these gradients are primarily influenced by the rotational component of the surface current, whereas the divergent component has a negligible impact (Bôas et al., 2020). That work identified a correlation between the spectral slopes of H_s and kinetic energy of ocean currents, suggesting a link between wave energy distribution and current dynamics — the spectral slope of H_s matches the spectral slope of the kinetic energy of the rotational component. Spatial gradients of H_s are more pronounced when the majority of the flow’s kinetic energy is concentrated in the rotational component.

The spatial variability in H_s is therefore connected with the components of the flow, or more precisely with their amount of vorticity. The wavenumber spectra of spatial variations of currents and H_s are shown in Figure 3. Spectra were computed along the main axis (E-W) in the black rectangle depicted in Figure 2 during the whole period of simulation at the wave model resolution of 4.4 km (Nyquist wavelength of 0.11 cpkm), after detrending the data. A Hann window was applied to the input matrix to minimize spectral leakage caused by discontinuities at the data boundaries. The window size was chosen to match the dimensions of the input matrix, using the same number of FFT elements as the original dataset, thereby preserving the spatial resolution of the analysis. To compensate for the energy attenuation inherent in windowing, the power spectral density was normalized by the total number of elements and the spatial resolution factors, ensuring an accurate representation of the total energy content in the wavenumber spectrum.

The H_s spectra (solid line) between wavelengths 100 and 35 km show a trend with slope about $k^{-2.5}$ over most of the wavenumber range. Beyond ~ 0.05 cpkm in Figure 3 the slope of the spectra become flat, possibly caused by the effective spatial resolution of the models. The current spectra is also shown in Figure 3, as a dashed line, with slopes and trends similar to the H_s spectra. The difference in the distribution of variance of H_s spectra with and without current input across the spatial scales is expected to be expressive. The H_s spectra without current input (the red dot-dashed line) is much less energetic and smoother in a region dominated by eddies. In the idealized simulations, a unimodal spectrum propagating in deep water without surface currents is likely to exhibit a highly homogeneous distribution of H_s . At spatial scales of 100 km, which are typical for eddies in this region, the disparity in wave energy between runs with and without current input reaches its maximum. At smaller scales, the difference diminishes progressively, as smaller eddies exhibit lower energy levels — Figure 2b.

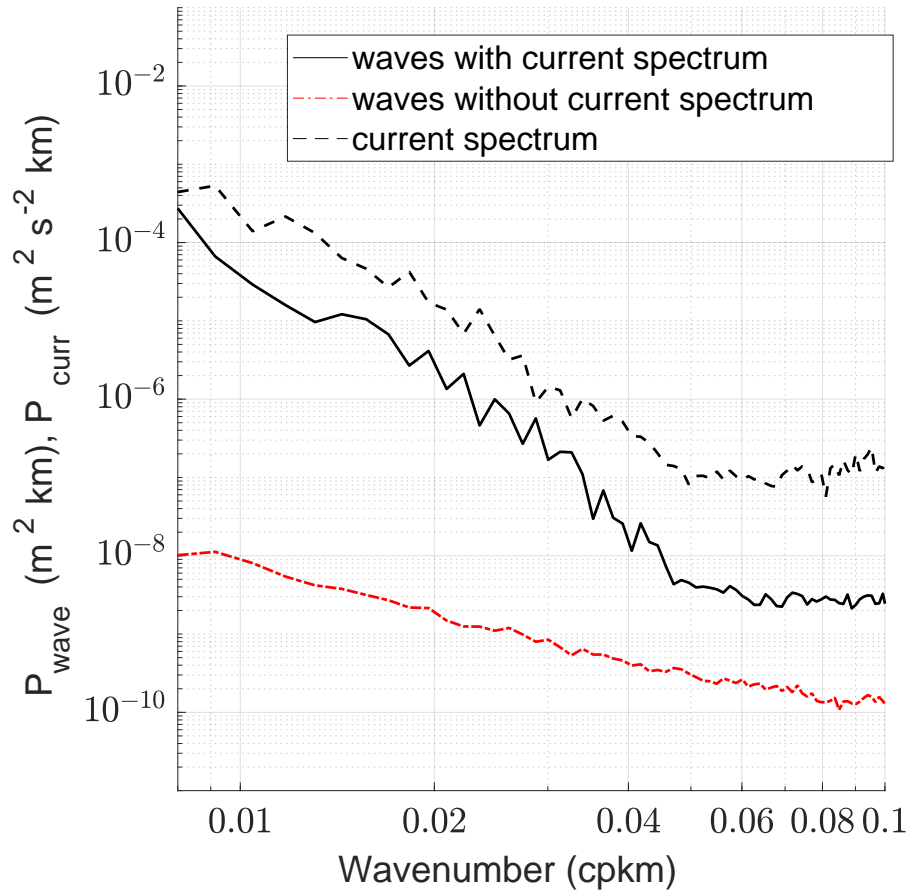


Figure 3: Averaged wavenumber spectra (in cycles per km) computed along the main axis (E-W) in the black rectangle in Figure 2 for H_s (solid line). The wavenumber H_s spectrum without current input is displayed in red. Averaged wavenumber spectrum of surface current speed is the dashed line.

4.2. Ocean Eddy Dipole in the Southwestern Atlantic Ocean

We now focus our attention on a two-month hindcast with a well developed dipole in the Southwestern Atlantic Ocean. Among the various tracks traversing the region, we selected only those in which the central jet maintained an approximately north–south orientation and with mainly southward

currents, typically in the opposite direction of swell (Violante-Carvalho et al., 2004). Under these circumstances, the current effects on waves are expected to cause the maximum amplification of H_s , as discussed in Section 2. The CCI- H_s data were employed to assess the response of the wave model to the different current inputs, listed in Table 1.

The South Brazilian Bight (SBB) is a geographical feature located off the coast of southern Brazil and known for the recurrent presence of ocean eddy dipoles (see a schematic representation in Figure 1). Within the meanders, the current can spawn swirling eddies, whose size ranges from a few kilometers to tens of kilometers and can persist for weeks or even months (Arruda and Silveira, 2019). The ocean circulation at the Sao Paulo plateau was addressed by Belo (2011) based on a series of measured current and hydrographic transects, indicating a pattern of successive eddy structures. According to Andrioni et al. (2012), dipoles are recurrent features as its surface signature can be frequently observed in satellite derived sea surface height in the region. Moreover, the Sao Paulo plateau acts as a natural eddy corridor where dipoles gradually move southwestward (de Paula et al., 2021).

The time evolution of some of the delayed-time merged ADT fields and derived absolute surface geostrophic velocities, from the SSalto/Duacs multi-mission altimeter data, are shown in Figure 4. The surface geostrophic currents from the ADT fields are one of three distinct input fields for the wave model. The low and high features that make up the asymmetric eddy dipole are highlighted within the black rectangle, with the satellite tracks superimposed. The side-by-side high and low ADT values characterize an eddy dipole, with adjacent anticyclonic and cyclonic eddies, respectively.

Figure 5, top row, shows the other two input current fields employed in the wave model runs, respectively GlobCurrent and HYCOM, for satellite track #4 in Table 1 — see also the ADT field in Figure 4b. The current fields shown in Figure 5 differ in magnitude and position of the maximum values, reflected in the relative difference in H_s between runs with and without current input displayed in the bottom row. The HYCOM currents are stronger than GlobCurrent (as generally expected) since the ageostrophic component is included, hence the relative differences in H_s are slightly more pronounced. HYCOM in this event misplaced the position of the central jet, even though the SSH field derived from altimeter data was incorporated during assimilation — the same altimeter data employed in the processing of SSalto and GlobCurrent.

H_s along the Jason-2 track are presented in Figure 6 (left) with the sev-

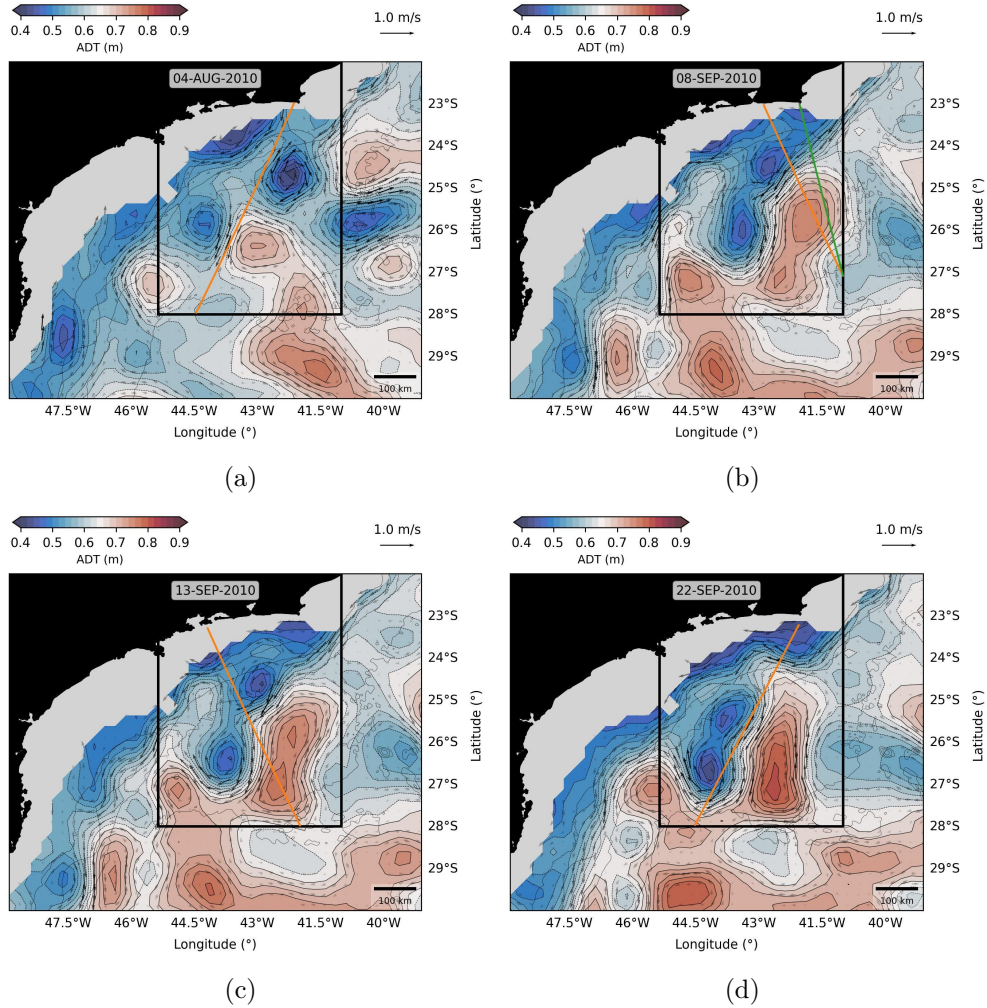


Figure 4: Fields of Absolute Dynamic Topography (ADT) from SSalto/Duacs and the derived geostrophic currents superimposed with the tracks shown as straight colored lines. [abcd] are four out of the 14 cases during the period of August and September 2010 that the satellite tracks crossed the dipole’s central jet, respectively tracks: #1; #4 and #5; #8; #13 (Table 1). The scale of the vectors is displayed on the top right corner.

eral runs of the wave model. Jason-2 measured a H_s maximum value of 3.5 m at 24.45°S, well spotted by SSalto and GlobCurrent runs (around 3.2 m) but missed in the simulation using the HYCOM input. SSalto and GlobCur-

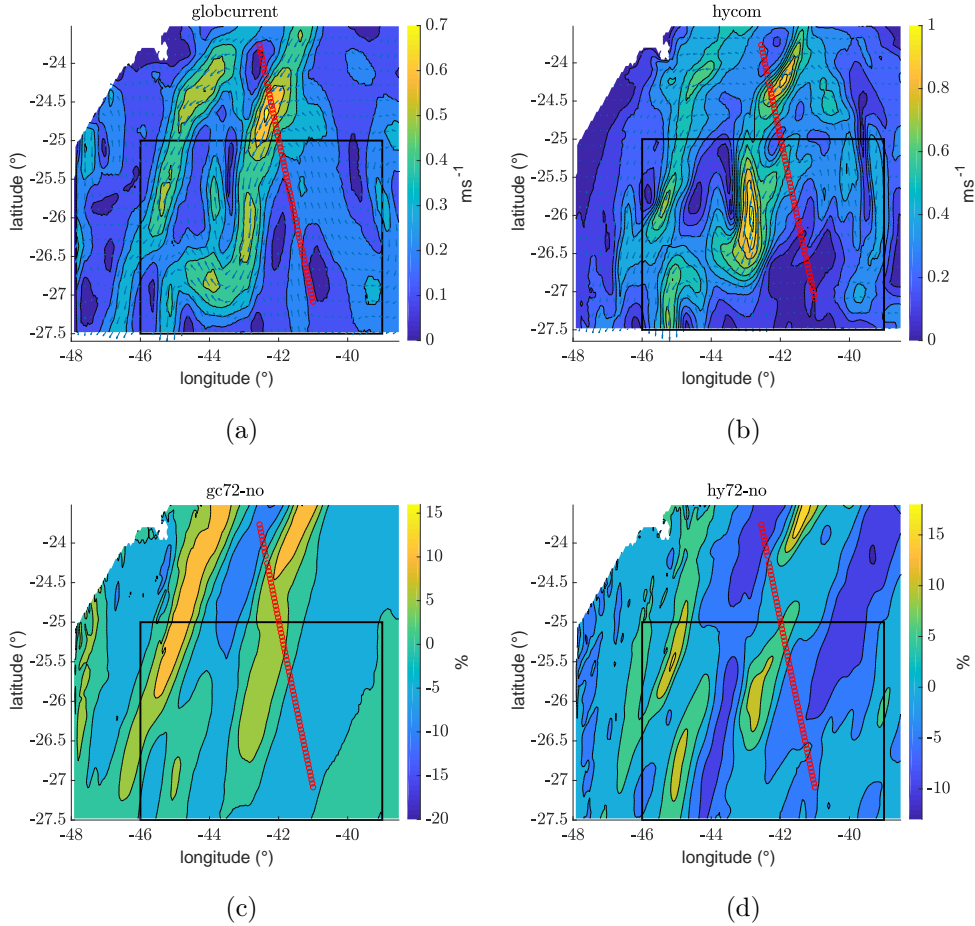


Figure 5: Example of one event that HYCOM misplaced the position of the strongest currents associated with the dipole — see also Figure 6. Top row: surface current field from GlobCurrent (left) and HYCOM (right) for 08-Sep-2010 at 07:00:00. The arrows indicate the current direction and magnitude sub-sampled every four bins. Red circles are the ground track of Jason-2 cycle 80. Bottom row: H_s relative difference between runs with and without current for GlobCurrent (left) and HYCOM (right). The results employing the SSalto current field are similar to GlobCurrent.

rent currents, interpolated along the satellite track (shown in Figure 6 top right and bottom right, respectively magnitude and direction), indicate both the same position of maximum values at 24.4°S . The addition of the Ek-

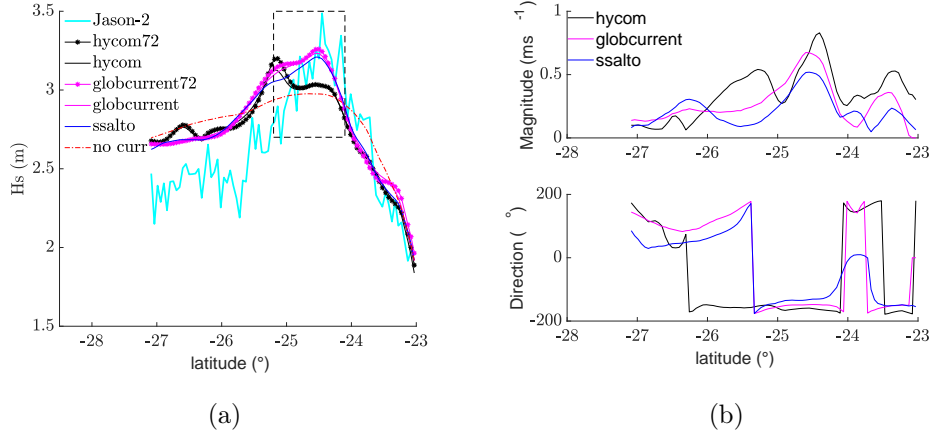


Figure 6: On the left, H_s along the Jason-2 track (for 08-Sep-2010 at around 07:07:00) including different wave model runs. The dashed rectangle is the region that the track crossed the dipole’s central jet. The ADT and derived geostrophic currents superimposed with the satellite track crossing the eddy dipole are shown in Figure 4b. On the right, magnitude (top) and direction (bottom) of the surface currents used as input for the wave model, interpolated along the track. Statistical parameters were also computed for each of the 14 track segments that crossed the dipole — see Table 2.

man component in GlobCurrent increased its magnitude but kept roughly the same position depicted in SSalto. HYCOM, however, misplaced the position of the maximum value by $\sim 20\text{-}30$ km. Although the magnitude is higher in HYCOM along the ground track, the simulated direction also differ from the ADT-derived currents. SSalto and Globcurrent are roughly south-southwestward, in the opposite direction of the north-northeastward swell, whereas HYCOM presents a more (orthogonal) westward component, hence with less influence on the wave propagation (Equation 1).

Another example of the misplacement of the central jet is illustrated in Figure 7, which can also be observed in the ADT field for satellite track #13 in Figure 4d (see Table 1 for reference). The current fields exhibit discrepancies in both magnitude and spatial positioning of their maximum values, which are reflected in the relative differences in H_s between simulations with and without current input. The left panel presents H_s measurements along the Jason-2 track, comparing them with multiple wave model runs. Jason-2 recorded a maximum H_s value of 2.9 m at 26.41°S, which was accurately cap-

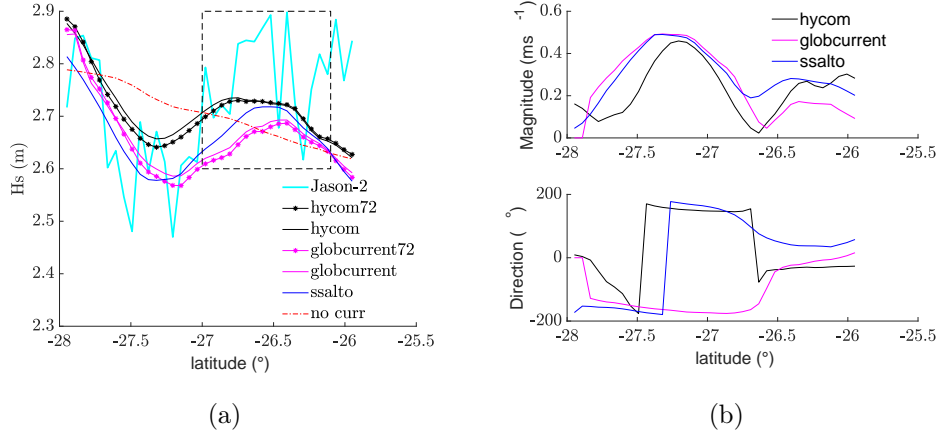


Figure 7: Same as Figure 6, for 22-Sep-2010 at around 14:40:00.

tured by the SSalto and GlobCurrent runs (with peaks around 2.7 m) but was missed by the simulation using HYCOM input. The SSalto and GlobCurrent current fields, when interpolated along the satellite track (shown in Figure 7, top right and bottom right, representing magnitude and direction, respectively), consistently identified the maximum value at 26.41°S. In contrast, HYCOM misplaced the position of the maximum value by approximately 30 km.

The primary reason for the greater mismatch of the eddy dipole simulated by global HYCOM, compared to derived gridded altimetry, is that the reanalysis assimilates along-track sea level anomalies. Although the reanalysis offers higher spatial resolution, the available tracks for assimilation cover smaller parts of the domain and may not have sampled the eddy dipole, thereby reducing the impact of data assimilation on correcting the position of this particular mesoscale feature. Additionally, all oceanic reanalyses contain other sources of error that contribute to deviations of global numerical simulations from the observed ocean state at regional scales. These include the lack of subsurface observations for assimilation, inaccuracies in topography representation, uncertainties in initial and boundary conditions, surface forcing, and limitations in the parameterizations used for sub-grid processes (Lima et al., 2019; de Souza et al., 2020; de Paula et al., 2021; Trott et al., 2023).

It is clear in Figure 6 and Figure 7 (left) that tripping the wave model

Table 2: Mean statistical parameters of H_s for the 14 selected ground tracks listed in Table 1. In black, the segments that crossed the dipole region (including the central jet) with a total of 971 points. In red, the segments that crossed the central jet only, with a total of 476 points. Respectively, CORR is the Pearson Correlation Coefficient, bias between model runs and altimeter, Root Mean Squared Error (RMSE), Scatter Index (SI) and Variance (VAR). HY72 is the run with the HYCOM surface current used as input for WW3 with a resolution of 72 directions, while HY if for 24 directions. GC72 is the run with the GlobCurrent surface current used as input for WW3 with a resolution of 72 directions, while GC is for 24 directions. SS is the run with the SSalto DUACS surface current used as input for WW3 with a resolution of 24 directions. NOC is the WW3 run without surface current as input

	CORR	BIAS (m)	RMSE (m)	SI (%)	VAR (m^2)
HY72	0.64 0.55	0.059 0.049	0.26 0.26	10.5 10.1	0.076 0.032
HY	0.64 0.57	0.062 0.043	0.26 0.26	10.4 9.9	0.072 0.025
GC72	0.66 0.61	0.039 0.026	0.24 0.24	9.8 9.2	0.062 0.026
GC	0.67 0.61	0.041 0.023	0.24 0.23	9.8 9.0	0.060 0.021
SS	0.68 0.65	0.040 0.022	0.23 0.22	9.4 8.6	0.057 0.022
NOC	0.53 0.30	0.040 -0.008	0.25 0.23	9.9 8.9	0.045 0.006

resolution from 24 to 72 directions has a marginal impact on H_s , despite the substantial increase in computing time. That is also evident considering the statistical parameters of the selected 14 tracks. The numbers in black in Table 2 correspond to the ground track segments that crossed the dipole region, with Figure 5 and Figure 6 as examples of the length of the segments of approximately 400 km each. These segments cross not only the dipole but the adjacent area, where the current field is less intense and hence less relevant for the wave field. The numbers in red correspond to the track segments of the much smaller central jet region, depicted as the dashed rectangle in Figure 6. As expected in such a dynamically complex region, correlation with the altimeter H_s considering the run with no current (dash-dotted red line in Figure 6) is low but with comparatively small RMSE, since the altimeter data go up and down relative to the much flatter no current H_s line. Results improve when considering the runs with currents as input, specially for SSalto and GlobCurrent (the latter with slightly poorer results). HYCOM surface currents, despite being physically more sound with the inclusion of the geostrophic component as input for the wave model, has worse results

caused by the greater difficulty of placing the currents on their correct positions. Both ADT-derived surface current inputs cause similar impacts on the wave field, with no substantial improvement with the inclusion of the Ekman component. Considering the dipole and its adjacent area (numbers in black), SSalto presents slightly better results. That is more evident considering the much more difficult task of placing correctly in space the comparatively small region of the central jet (numbers in red). The correlation coefficient is a good indicator whether the H_s curves move together consistently, with the SSalto current input presenting a correlation coefficient of 65% with the altimeter data, ten points greater than HYCOM. Additionally, the biases observed in HYCOM simulations are twice as large as those in the SSalto simulations — however, the differences in RMSE are not statistically significant. HYCOM is particularly effective in capturing a broad range of dynamical processes, including ageostrophic and smaller-scale components essential for accurate ocean energy representation. However, discrepancies with gridded SSalto/-Duacs data may arise from potential assimilation inaccuracies and inherent model limitations, such as parameterization errors and uncertainties in atmospheric forcing.

Wavenumber spectra were computed for the month of September, shown in Figure 8, following the same procedure described in Section 4.1 — solid lines for H_s and dashed lines for current speeds. In the range from 100 to 30 km, the current spectrum from HYCOM is more energetic (dashed black) than SSalto (dashed blue) and GlobCurrent (dashed magenta), which show similar patterns. The difference in energy at the lower wavenumber band between current spectra from HYCOM and from the ADT-derived field could be partially attributed to the ageostrophic component, not present in SSalto and GlobCurrent (although the latter includes the Ekman component). The surface current grid derived from the composition of several altimeter tracks with a course time resolution of 24 hours is expected to be smoother, which could also add to the discrepancy in spectral energy. The surface currents were interpolated to match the wave model’s resolution of 4.4 km. However, SSalto and GlobCurrent datasets have a coarser spatial resolution of 25 km, compared to HYCOM’s 9 km. Consequently, interpretations of the spectral behaviour beyond ~ 0.02 cpkm — specially for the ADT-derived currents — should be approached with caution.

The slopes of the H_s spectra (solid lines) are similar to the current spectra, with the HYCOM currents as input (solid black) also exhibiting higher spatial variability compared to SSalto (solid blue) and GlobCurrent (solid

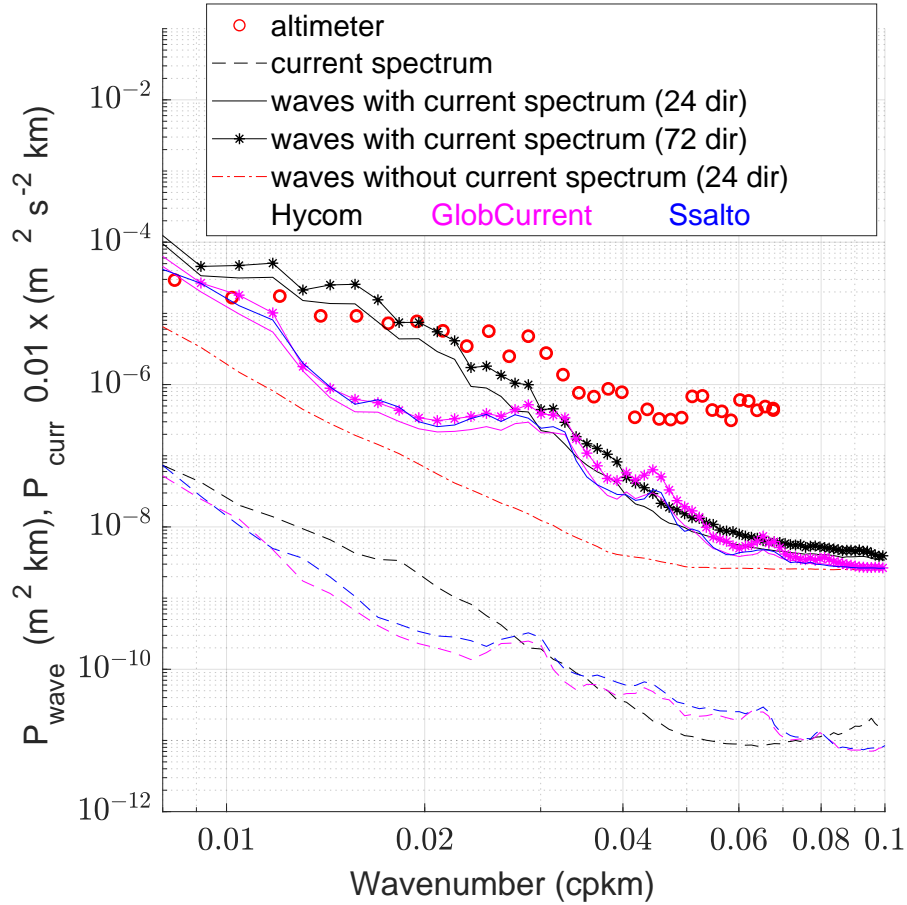


Figure 8: Wavenumber spectra (in cycles per km) computed along the main axis (E-W) in the black rectangle in Figure 5 for H_s (solid lines) averaged for the month of September. The wavenumber H_s spectrum without current input is displayed as the dash-dotted red line. For comparison, the along-track averaged spectrum corresponding to all tracks listed in Table 1 are presented as red circles. Averaged wavenumber spectra of surface current speed are the dashed lines — scaled by a factor 10^{-2} for easy of visualization.

magenta). Notably, there are striking differences in the spectral content between the runs with and without current input (dash-dotted red line).

Tripping the directional spectrum results in a minor increase in the spectral content. Similar to the current spectra, all the H_s spectra converge at approximately 0.03 cpkm. The averaged along-track spectrum for all tracks listed in Table 1 is presented as red circles, illustrating the spatial variability of H_s along the altimeter tracks. The wavenumber spectrum of H_s shows strong agreement with our model results, particularly with simulations that incorporate ocean current effects from HYCOM. At wavelengths shorter than 50 km, the altimeter data are influenced by high-frequency noise, resulting in a nearly flat spectrum for wavenumbers greater than 0.02 cpkm. Although comparing the H_s spectra generated from different current fields used as input to the wave model is not straightforward, it offers an interesting opportunity to infer distinct responses of the wave field to the various components of the surface currents. The surface current from HYCOM is expected to be more energetic, not only due to the presence of the ageostrophic component but also because of the comparatively less smoothed currents. Consequently, the H_s spectrum using the HYCOM input is also expected to be more energetic at lower wavenumbers.

5. Summary and Conclusions

We investigate the influence of surface currents on the spatial variability of the wave field in the vicinity of an ocean eddy dipole. Eddy dipoles are ubiquitous mesoscale features in the oceans, characterized by adjacent cyclonic and anticyclonic, counter-rotating eddies separated by a central jet. These structures can form in regions dominated by intense currents as well as in areas characterized by relatively weak flow regimes. An idealized setup using the WW3 wave model was employed to analyze the impact on significant wave height (H_s). Additionally, a two-month hindcast of an intense dipole event in the Southwestern Atlantic Ocean was conducted using three distinct surface current fields — HYCOM, GlobCurrent, and SSalto/Duacs — as input to the WW3 model. The results underscore the sensitivity of wave fields to different current components, with significant variations in wave amplification observed across the various current inputs. HYCOM, incorporating ageostrophic effects and dynamic interpolation of surface currents, provided a more detailed representation of ocean surface dynamics. In contrast, GlobCurrent and SSalto/Duacs, derived from altimeter data, primarily captured the geostrophic component, with GlobCurrent also including the Ekman component. The hindcast was assessed using denoised

altimeter-derived H_s data at a spatial resolution of approximately 6 km — the high-resolution data allows for a detailed assessment of wave variability.

In the idealized simulations, a substantial increase in H_s is observed in the central jet within regions of maximum opposing surface currents. Dipoles function as converging lenses for surface waves, effectively directing their refraction toward the central jet. The combined effects of wave refraction and advection significantly enhance wave energy and steepness over the central jet, with shorter period waves exhibiting more significant alterations in both height and steepness compared to longer period waves. A substantial difference is observed in the variance distribution of H_s spectra across various spatial scales when comparing conditions with and without current input. The H_s spectrum without current input exhibits significantly lower energy — the variance is markedly more pronounced when currents are included into the simulations, highlighting the dynamic interplay between waves and surface currents in the vicinity of eddy dipoles.

The hindcast results indicate that the surface current from SSalto-Duacs, despite its poorer spatial and temporal resolutions, yields more reliable H_s fields. Surface current inputs derived from ADT produce comparable effects on the wave field, with the inclusion of the Ekman component yielding no significant enhancement. HYCOM’s advantage lies in its ability to capture a wide range of dynamical processes, including ageostrophic and smaller-scale components, which are critical for accurately representing the total energy in the ocean. Discrepancies between the HYCOM model and the gridded SSalto/Duacs data could arise due to potential inaccuracies in the assimilation process. In addition to assimilation issues, every numerical model has inherent limitations, including the parameterization of sub-grid processes, errors and uncertainties in atmospheric forcing and numerical approximations — all of which contribute to the overall accuracy and reliability of the model output. While HYCOM might be less precise spatially, it provides a more comprehensive and statistically robust representation of oceanic energy dynamics. Although gridded altimetry might underestimate the total current components associated with eddy dipole events, it can offer a more precise representation of their position and evolution, which is particularly relevant for analyzing specific events and near real-time forecasting.

Acknowledgments

NVC was partially supported by the Rio de Janeiro's Science Foundation (FAPERJ) under Grant Number APQ1-13/2023-293444.

References

- Altiparmaki, O., Breivik, O., Aouf, L., Bohlinger, P., Johannessen, J.A., Collard, F., Donlon, C., Hope, G., Visser, P.N.A.M., Naeije, M., 2024. Influence of ocean currents on wave modeling and satellite observations: Insights from the one ocean expedition. *Journal of Geophysical Research: Oceans* 129, e2024JC021581. URL: <https://agupubs.onlinelibrary.wiley.com/doi/abs/10.1029/2024JC021581>, doi:<https://doi.org/10.1029/2024JC021581>. e2024JC021581 2024JC021581.
- Amante, C., Eakins, B.W., 2009. Etopo1 1 arc-minute global relief model: procedures, data sources and analysis. URL: <https://doi.org/10.1594/PANGAEA.769615>, doi:10.1594/PANGAEA.769615. NOAA technical memorandum. National Geophysical Data Center.
- Andrioni, M., Moreira Lima, J.A., Guerra, L.A., Ribeiro, E.O., Paiva Nunes, L.M., Ceccopieri, W., de Souza Rego, V., de Oliveira, S.M., 2012. Ocean eddies' influence on lula field, santos basin, Brazil, in: *International Conference on Offshore Mechanics and Arctic Engineering*, pp. 189–193. URL: <https://doi.org/10.1115/OMAE2012-83480>, doi:10.1115/OMAE2012-83480.
- Ardhuin, F., Gille, S.T., Menemenlis, D., Rocha, C.B., Rasche, N., Chapron, B., Gula, J., Molemaker, J., 2017. Small-scale open ocean currents have large effects on wind wave heights. *Journal of Geophysical Research: Oceans* 122, 4500–4517. URL: <https://agupubs.onlinelibrary.wiley.com/doi/abs/10.1002/2016JC012413>, doi:<https://doi.org/10.1002/2016JC012413>.
- Ardhuin, F., Rogers, E., Babanin, A.V., Filipot, J.F., Magne, R., Roland, A., van der Westhuysen, A., Queffelec, P., Lefevre, J.M., Aouf, L., Collard, F., 2010. Semiempirical dissipation source functions for ocean waves. part i: Definition, calibration, and validation. *Journal of Physical Oceanography* 40, 1917 – 1941. URL: <https://journals.ametsoc.org/view/journals/phoc/40/9/2010jpo4324.1.xml>, doi:<https://doi.org/10.1175/2010JP04324.1>.
- Ardhuin, F., Roland, A., Dumas, F., Bennis, A.C., Sentchev, A., Forget, P., Wolf, J., Girard, F., Osuna, P., Benoit, M., 2012. Numerical wave modeling in conditions with strong currents: Dissipa-

- tion, refraction, and relative wind. *Journal of Physical Oceanography* 42, 2101 – 2120. URL: <https://journals.ametsoc.org/view/journals/phoc/42/12/jpo-d-11-0220.1.xml>, doi:<https://doi.org/10.1175/JPO-D-11-0220.1>.
- Arruda, W.Z., Silveira, I., 2019. Dipole-induced central water extrusions south of Abrolhos Bank (Brazil, 20.5°s). *Continental Shelf Research* 188, 103976.
- Belo, W.C., 2011. The Inner Recirculation of the South Atlantic Subtropical Gyre and the Oceanic Circulation on the Pre-Salt Cluster Region in the Santos Basin. Phd thesis. University of São Paulo. São Paulo, SP, Brazil. doi:10.11606/T.21.2011.tde-20042012-152310. available at <https://www.teses.usp.br/teses/disponiveis/21/21132/tde-20042012-152310/en.php>.
- Benetazzo, A., Carniel, S., Sclavo, M., Bergamasco, A., 2013. Wave–current interaction: Effect on the wave field in a semi-enclosed basin. *Ocean Modelling* 70, 152–165. URL: <https://www.sciencedirect.com/science/article/pii/S1463500312001862>, doi:<https://doi.org/10.1016/j.ocemod.2012.12.009>.
- Biló, T.C., da Silveira, I.C.A., Belo, W.C., de Castro, B.M., Piola, A.R., 2014. Methods for estimating the velocities of the Brazil current in the pre-salt reservoir area off southeast Brazil (23s–26s). *Ocean Dynamics* 64, 1431–1446. URL: <https://doi.org/10.1007/s10236-014-0761-2>, doi:10.1007/s10236-014-0761-2.
- Bôas, A.B.V., Cornuelle, B.D., Mazloff, M.R., Gille, S.T., Arduin, F., 2020. Wave–current interactions at meso- and submesoscales: Insights from idealized numerical simulations. *Journal of Physical Oceanography* 50, 3483 – 3500. URL: <https://journals.ametsoc.org/view/journals/phoc/50/12/JPO-D-20-0151.1.xml>, doi:<https://doi.org/10.1175/JPO-D-20-0151.1>.
- Calado, L., Gangopadhyay, A., Silveira, I., 2006. A parametric model for the Brazil current meanders and eddies off southeastern Brazil. *Geophysical research letters* 33.

- Campos, E., Velhote, D., da Silveira, I., 2000. Shelf break upwelling driven by Brazil current cyclonic meanders. *Geophysical Research Letters* 27, 751–754. URL: <https://agupubs.onlinelibrary.wiley.com/doi/abs/10.1029/1999GL010502>, doi:10.1029/1999GL010502.
- Cancet, M., Griffin, D., Cahill, M., Chapron, B., Johannessen, J., Donlon, C., 2019. Evaluation of globcurrent surface ocean current products: A case study in Australia. *Remote sensing of environment* 220, 71–93.
- Chassignet, E.P., Hurlburt, H.E., Metzger, E.J., Smedstad, O.M., Cummings, J.A., Halliwell, G.R., Bleck, R., Baraille, R., Wallcraft, A.J., Lozano, C., et al., 2009. Us godae: global ocean prediction with the hybrid coordinate ocean model (HYCOM). *Oceanography* 22, 64–75.
- Chassignet, E.P., Hurlburt, H.E., Smedstad, O.M., Halliwell, G.R., Hogan, P.J., Wallcraft, A.J., Bleck, R., 2006. Ocean prediction with the hybrid coordinate ocean model (HYCOM). *Ocean weather forecasting: an integrated view of oceanography* , 413–426.
- de Paula, T.P., Lima, J.A.M., Tanajura, C.A.S., Andrioni, M., Martins, R.P., Arruda, W.Z., 2021. The impact of ocean data assimilation on the simulation of mesoscale eddies at São Paulo Plateau (Brazil) using the regional ocean modeling system. *Ocean Modelling* 167, 101889. URL: <https://www.sciencedirect.com/science/article/pii/S1463500321001426>, doi:<https://doi.org/10.1016/j.ocemod.2021.101889>.
- Dodet, G., Piolle, J.F., Quilfen, Y., Abdalla, S., Accensi, M., Arduin, F., Ash, E., Bidlot, J.R., Gommenginger, C., Marechal, G., Passaro, M., Quartly, G., Stopa, J., Timmermans, B., Young, I., Cipollini, P., Donlon, C., 2020. The Sea State CCI dataset v1: towards a sea state climate data record based on satellite observations. *Earth System Science Data* 12, 1929–1951. URL: <https://essd.copernicus.org/articles/12/1929/2020/>, doi:10.5194/essd-12-1929-2020.
- Dysthe, K.B., 2001. Refraction of gravity waves by weak current gradients. *Journal of Fluid Mechanics* 442, 157–159. doi:10.1017/S0022112001005237.

- Echevarria, E.R., Hemer, M.A., Holbrook, N.J., 2021. Global implications of surface current modulation of the wind-wave field. *Ocean Modelling* 161, 101792. URL: <https://www.sciencedirect.com/science/article/pii/S1463500321000421>, doi:<https://doi.org/10.1016/j.ocemod.2021.101792>.
- Fox, D.N., Barron, C.N., Carnes, M.R., Booda, M., Peggion, G., Van Gurley, J., 2002. The modular ocean data assimilation system. *Oceanography* 15, 22–28.
- Gallet, B., Young, W.R., 2014. Refraction of swell by surface currents. *J. Mar. Res.* 72, 105–126. URL: <https://doi.org/10.1357/002224014813758959>.
- Gula, J., Taylor, J., Shcherbina, A., Mahadevan, A., 2022. Chapter 8 - sub-mesoscale processes and mixing, in: Meredith, M., Naveira Garabato, A. (Eds.), *Ocean Mixing*. Elsevier, pp. 181–214. URL: <https://www.sciencedirect.com/science/article/pii/B9780128215128000153>, doi:<https://doi.org/10.1016/B978-0-12-821512-8.00015-3>.
- Huang, N.E., Shen, Z., Long, S.R., Wu, M.C., Shih, H.H., Zheng, Q., Yen, N.C., Tung, C.C., Liu, H.H., 1998. The empirical mode decomposition and the hilbert spectrum for non-linear and non-stationary time series analysis. *Proceedings of the Royal Society of London* 454, 903–995. URL: <https://doi.org/10.1098/rspa.1998.0193>, doi:10.1098/rspa.1998.0193, arXiv:<https://doi.org/10.1098/rspa.1998.0193>.
- Kaiser, J., Nogueira, I.C.M., Campos, R.M., et al., 2022. Evaluation of wave model performance in the South Atlantic Ocean: A study about physical parameterization and wind forcing calibration. *Ocean Dynamics* 72, 137–150. URL: <https://doi.org/10.1007/s10236-021-01495-4>, doi:10.1007/s10236-021-01495-4.
- Kenyon, K.E., 1971. Wave refraction in ocean currents. *Deep Sea Research and Oceanographic Abstracts* 18, 1023–1034. URL: <https://www.sciencedirect.com/science/article/pii/0011747171900064>, doi:[https://doi.org/10.1016/0011-7471\(71\)90006-4](https://doi.org/10.1016/0011-7471(71)90006-4).

- Lauton, G., Marta-Almeida, M., Lentini, C.A.D., 2023. The effect of currents on large surface gravity waves under cyclonic conditions in the south/southeastern Brazil. *Journal of Geophysical Research: Oceans* 128, e2022JC018472. URL: <https://agupubs.onlinelibrary.wiley.com/doi/abs/10.1029/2022JC018472>, doi:<https://doi.org/10.1029/2022JC018472>. e2022JC018472 2022JC018472.
- Lima, L.N., Pezzi, L.P., Penny, S.G., Tanajura, C.A.S., 2019. An investigation of ocean model uncertainties through ensemble forecast experiments in the southwest Atlantic Ocean. *Journal of Geophysical Research: Oceans* 124. URL: <http://dx.doi.org/10.1029/2018JC013919>, doi:10.1029/2018JC013919.
- Marechal, G., Ardhuin, F., 2021. Surface currents and significant wave height gradients: Matching numerical models and high-resolution altimeter wave heights in the agulhas current region. *Journal of Geophysical Research: Oceans* 126, e2020JC016564. URL: <https://agupubs.onlinelibrary.wiley.com/doi/abs/10.1029/2020JC016564>, doi:<https://doi.org/10.1029/2020JC016564>. e2020JC016564 2020JC016564.
- Mertz, F., Germineaud, C., Soudarin, L., Rosmorduc, V., Schgounn, C., Birol, F., Niño, F., Guinle, T., 2023. Aviso+: what's new on the reference portal in satellite altimetry?, in: EGU General Assembly Conference Abstracts, pp. EGU–17412.
- Moreira, R.M., Peregrine, D.H., 2012. Nonlinear interactions between deep-water waves and currents. *Journal of Fluid Mechanics* 691, 1–25. doi:10.1017/jfm.2011.436.
- Munk, W.H., Miller, G.R., Snodgrass, F.E., Barber, N.F., Deacon, G.E.R., 1963. Directional recording of swell from distant storms. *Philosophical Transactions of the Royal Society of London. Series A, Mathematical and Physical Sciences* 255, 505–584. URL: <https://royalsocietypublishing.org/doi/abs/10.1098/rsta.1963.0011>, doi:10.1098/rsta.1963.0011.
- Ni, Q., Zhai, X., Wang, G., Hughes, C.W., 2020. Widespread mesoscale dipoles in the global ocean. *Journal of Geophysical Research: Oceans* 125, e2020JC016479. URL: <https://agupubs.onlinelibrary.wiley.com/doi/abs/10.1029/2020JC016479>.

wiley.com/doi/abs/10.1029/2020JC016479, doi:<https://doi.org/10.1029/2020JC016479>. e2020JC016479 2020JC016479.

- Onorato, M., Osborne, A.R., Serio, M., 2002. Extreme wave events in directional, random oceanic sea states. *Physics of Fluids* 14, L25–L28. URL: <https://doi.org/10.1063/1.1453466>, doi:10.1063/1.1453466, arXiv:<https://doi.org/10.1063/1.1453466>.
- Onorato, M., Proment, D., Toffoli, A., 2011. Triggering rogue waves in opposing currents. *Physical Review Letters* 107. URL: <https://doi.org/10.1103/PhysRevLett.107.184502>, doi:10.1103/PhysRevLett.107.184502.
- Peregrine, D., 1976. Interaction of water waves and currents, in: Yih, C.S. (Ed.), *Advances in Applied Mechanics*. Elsevier. volume 16, pp. 9–117. URL: <https://www.sciencedirect.com/science/article/pii/S0065215608700875>, doi:[https://doi.org/10.1016/S0065-2156\(08\)70087-5](https://doi.org/10.1016/S0065-2156(08)70087-5).
- Phillips, O.M., 1977. *The dynamics of the upper ocean*. Second Edition, Cambridge University Press .
- Piollé, J.F., Dodet, G., Quilfen, Y., 2022. ESA Sea State Climate Change Initiative (Sea_State_CCI) : Global remote sensing daily merged multi-mission along-track significant wave height from altimetry, l3 product, version 3. NERC EDS Centre for Environmental Data Analysis URL: <https://dx.doi.org/10.5285/e6af67fca81c40b7bb3eddaadde06909>, doi:10.5285/e6af67fca81c40b7bb3eddaadde06909.
- Quilfen, Y., Chapron, B., 2019. Ocean surface wave-current signatures from satellite altimeter measurements. *Geophysical Research Letters* 46, 253–261. URL: <https://agupubs.onlinelibrary.wiley.com/doi/abs/10.1029/2018GL081029>, doi:<https://doi.org/10.1029/2018GL081029>.
- Quilfen, Y., Yurovskaya, M., Chapron, B., Ardhuin, F., 2018a. Storm waves focusing and steepening in the agulhas current: Satellite observations and modeling. *Remote Sensing of Environment* 216, 561–571. URL: <https://www.sciencedirect.com/science/article/pii/S0034425718300000>.

- S0034425718303535, doi:<https://doi.org/10.1016/j.rse.2018.07.020>.
- Quilfen, Y., Yurovskaya, M., Chapron, B., Ardhuin, F., 2018b. Storm waves focusing and steepening in the agulhas current: Satellite observations and modeling. *Remote Sensing of Environment* 216, 561–571. URL: <https://www.sciencedirect.com/science/article/pii/S0034425718303535>, doi:<https://doi.org/10.1016/j.rse.2018.07.020>.
- Rio, M.H., Mulet, S., Picot, N., 2014. Beyond goce for the ocean circulation estimate: Synergetic use of altimetry, gravimetry, and in situ data provides new insight into geostrophic and ekman currents. *Geophysical Research Letters* 41, 8918–8925. URL: <https://agupubs.onlinelibrary.wiley.com/doi/abs/10.1002/2014GL061773>, doi:<https://doi.org/10.1002/2014GL061773>.
- Rocha, C.B., Silveira, I.C.A., Castro, B.M., Lima, J.A.M., 2014. Vertical structure, energetics, and dynamics of the Brazil current system at 22°s–28°s. *Journal of Geophysical Research: Oceans* 119, 52–69. URL: <https://agupubs.onlinelibrary.wiley.com/doi/abs/10.1002/2013JC009143>, doi:<https://doi.org/10.1002/2013JC009143>.
- Romero, L., Hypolite, D., McWilliams, J.C., 2020. Submesoscale current effects on surface waves. *Ocean Modelling* 153, 101662. URL: <https://www.sciencedirect.com/science/article/pii/S1463500320301645>, doi:<https://doi.org/10.1016/j.ocemod.2020.101662>.
- Romero, L., Lenain, L., Melville, W.K., 2017. Observations of surface wave–current interaction. *Journal of Physical Oceanography* 47, 615 – 632. URL: <https://journals.ametsoc.org/view/journals/phoc/47/3/jpo-d-16-0108.1.xml>, doi:<https://doi.org/10.1175/JPO-D-16-0108.1>.
- Sandwell, D.T., Müller, R.D., Smith, W.H.F., Garcia, E., Francis, R., 2014. New global marine gravity model from cryosat-2 and jason-1 reveals buried tectonic structure. *Science* 346, 65–67. URL: <https://www.science.org/doi/abs/10.1126/science.1258213>, doi:10.1126/science.1258213.

- Silveira, I., Lima, J., Schmidt, A., Ceccopieri, W., Sartori, A., Francisco, C., Fontes, R., 2008. Is the meander growth in the Brazil current system off southeast Brazil due to baroclinic instability? *Dynamics of Atmospheres and Oceans* 45, 187–207. URL: <https://www.sciencedirect.com/science/article/pii/S037702650800033X>, doi:<https://doi.org/10.1016/j.dynatmoce.2008.01.002>. oCEANIC FRONTS.
- Silveira, I., Pereira, F., Flierl, G.R., Simoes Sousa, I.T., Palóczy, A., Borges-Silva, M., Rocha, C.B., 2023. The Brazil current quasi-stationary unstable meanders at 22° s–23° s. *Progress in Oceanography* 210, 102925.
- de Souza, J.M.A.C., Couto, P., Soutelino, R., Roughan, M., 2020. Evaluation of four global ocean reanalysis products for new zealand waters—a guide for regional ocean modelling. *New Zealand Journal of Marine and Freshwater Research* 55, 132–155. URL: <https://doi.org/10.1080/00288330.2020.1713179>, doi:10.1080/00288330.2020.1713179.
- Toffoli, A., Waseda, T., Houtani, H., Cavaleri, L., Greaves, D., Onorato, M., 2015. Rogue waves in opposing currents: an experimental study on deterministic and stochastic wave trains. *Journal of Fluid Mechanics* 769, 277–297. doi:10.1017/jfm.2015.132.
- Trott, C.B., Metzger, E.J., Yu, Z., 2023. Luzon strait mesoscale eddy characteristics in HYCOM reanalysis, simulation, and forecasts. *Journal of Oceanography* 79, 423–441. URL: <https://doi.org/10.1007/s10872-023-00686-5>, doi:10.1007/s10872-023-00686-5.
- Violante-Carvalho, N., Arruda, W.Z., Carvalho, L.M., Rogers, W.E., Passaro, M., 2021. Diffraction of irregular ocean waves measured by altimeter in the lee of islands. *Remote Sensing of Environment* 265, 112653. URL: <https://www.sciencedirect.com/science/article/pii/S0034425721003734>, doi:<https://doi.org/10.1016/j.rse.2021.112653>.
- Violante-Carvalho, N., Ocampo-Torres, F., Robinson, I., 2004. Buoy observations of the influence of swell on wind waves in the open ocean. *Applied Ocean Research* 26, 49–60. URL: <https://www.sciencedirect.com/science/article/pii/S0141118704000367>, doi:<https://doi.org/10.1016/j.apor.2003.11.002>.

WW3DG, 2019. User manual and system documentation of WAVEWATCH III version 6.07. NOAA/NWS/NCEP/MMAB. , College Park, MD, USA, WAVEWATCH III Development Group, Tech. Note 326 pp.